


Electron-momentum-spectroscopy study on the valence electronic structure of methyl iodide: Electron correlation and relativistic effects

Shanshan Niu, Yaguo Tang,^{*} Zhaohui Liu, Yufeng Shi, Enliang Wang, Xu Shan,[†] and Xiangjun Chen
*Hefei National Laboratory for Physical Sciences at the Microscale and Department of Modern Physics,
 University of Science and Technology of China, Hefei, Anhui 230026, China*

 (Received 9 January 2019; revised manuscript received 4 February 2019; published 25 February 2019)

We report an experimental and theoretical study on the electronic structure of methyl iodide. The binding energy spectrum (BES) and electron-momentum profiles (EMPs) of valence orbitals have been measured using a high-sensitivity electron-momentum spectrometer at the impact energy of 1200 eV plus binding energy. Theoretical calculations considering the relativistic and electron correlation effects are performed to illuminate the measured results. For the two outermost orbitals, the relativistic effects are revealed by the experimental and theoretical EMPs for two spin-orbit splitting components ($2e_{3/2}$ and $2e_{1/2}$) and the C-I bonding orbital ($3a_1$). In the inner valence region, satellite structures associated with the ionizations from $2a_1$ and $1a_1$ orbitals are observed in the BES and the pole strengths for the satellites are determined by comparing the measured EMPs with the calculated ones. Moreover, distinct relativistic and electron correlation effects on the EMPs for the $2a_1$ orbital and its satellites have been found.

DOI: [10.1103/PhysRevA.99.022512](https://doi.org/10.1103/PhysRevA.99.022512)

I. INTRODUCTION

Electron-momentum spectroscopy (EMS), also known as binary ($e, 2e$) spectroscopy, is based on kinematically complete electron-impact ionization experiments in which a fast projectile electron is used to eject a bound electron from an atomic or molecular target with the simultaneous detection of the two outgoing electrons (scattered and ejected) in the energy and angular domains [1–4]. The incident electron energy is usually high (typically 1.2 keV) to enable a binary encounter between the projectile and bound electron of the target in the ionization, so that we can probe the target electronic structure. The unique ability of EMS lies in directly measuring the binding energy spectrum (BES) and electron-momentum profiles (EMPs) for individual orbitals at the same time. Such information is essential knowledge to understand the motion and correlation of valence electrons in atoms, molecules, and their ions. For the outer valence orbitals, the experimental results for their single-hole states can be well interpreted by the calculations based on the independent-particle model. However, in the inner valence region satellite structures (or bands) often appear associated with the ionization and shake-up excitation processes of orbital electrons, which may make the independent-particle model invalid. The mechanism of the shake-up process can be interpreted by the configuration interaction (CI) between the single-hole configurations and the two-hole–one-particle ($2h - 1p$) or even higher excited configurations in the final ion states, which is the result of electron correlation effects [5–10]. Therefore, satellite states offer a system suitable for the investigation of many-body electron correlation. EMS allows one to ascertain

unambiguously the symmetry of the ionization states and to measure the probability of the redistribution of the intensity associated with the single-hole configuration over other ionic configurations. Consequently, the observed EMPs, together with the corresponding theoretical calculations, have offered a more straightforward way for the accurate assignment and the determination of the pole strengths of the satellite states [4,10–22].

In the case of heavy atoms and molecules containing heavy atoms, relativistic effects may become important for valence electrons and play a distinct role in ionization energies and wave functions of valence orbitals which are crucial for understanding the physical and chemical properties of matter [23–25]. Since the pioneering work of Cook *et al.* [26], EMS has been applied to explore relativistic effects on electron wave functions of heavy atoms [26–30], and particularly to the spin-orbit coupling revealed by the measured branching ratio of two splitting components with the aid of calculations using Dirac-Fock theory. However, relativistic EMS studies for molecular targets are scarce [31–34]. Li *et al.* [31] reported an experiment about the relativistic effect on the highest occupied molecular orbital (HOMO) of CF_3I which is essentially an I $5p$ lone pair orbital. Subsequently, Ning and co-workers reported the relativistic EMS studies for I_2 molecule [32,33] and Wang *et al.* presented the relativistic effect on the HOMO of n -propyl iodide [34] with the help of relativistic calculations by the Amsterdam density functional (ADF) method [35,36]. It is necessary to further extend EMS application on this issue to more molecules containing heavy elements.

Methyl iodide (CH_3I), a prototype molecule containing heavy elements, is used widely as a methylation reagent in organic synthesis. Relativistic effects caused by the high- Z iodine atom ($Z = 53$) and electron correlation effects may occur in valence orbitals. The ionization bands of CH_3I associated with the outer valence single-hole states have

^{*}tang2516@ustc.edu.cn

[†]xshan@ustc.edu.cn

been thoroughly characterized by photoelectron spectra (PES) [37–42] and the band of the $2e$ orbital (HOMO) was observed to split into $2e_{3/2}$ and $2e_{1/2}$ components which is the result of spin-orbit coupling effects. Satellite structures associated with ionizations from the inner valence orbitals have also been observed and assigned with the aid of theoretical predictions [41,42]. There was only an early EMS experiment on CH_3I conducted by Minchinton *et al.* [43] in 1985. They presented the BES and the EMPs for the valence orbitals. However, at that time, limited to the poor experimental statistics and the calculation by Hartree-Fock (HF) method with small basis sets, large discrepancies between experimental and theoretical EMPs existed in the low-momentum region. It is therefore necessary to carry out a high-sensitivity EMS measurement and comprehensive calculations considering relativistic effects and electron correlation effects to reinvestigate the valence electronic structure of CH_3I .

In this work, we report an EMS experiment of CH_3I using a high-sensitivity EMS spectrometer. The BES is measured, from which three well-resolved bands and several satellite structures are observed in the outer and inner valence ionization region. The experimental EMPs for valence orbitals and the satellites have been obtained. The theoretical EMPs are calculated by nonrelativistic and spin-orbit relativistic methods as well as relativistic pseudopotential basis sets to investigate the relativistic effects in CH_3I . The pole strengths of the main states and the satellites are determined by comparing the experimental EMPs with the theoretical ones. Combined with the symmetry-adapted-cluster configuration-interaction (SAC-CI) general- R [44–47] calculation, many-body electron correlation effects are also analyzed.

II. EXPERIMENTAL AND THEORETICAL BACKGROUND

EMS is based on the electron-impact ionization of a target atom or molecule which can be described completely by the $(e, 2e)$ reaction,

$$e_0(E_0, \mathbf{p}_0) + M \rightarrow M^+ + e_1(E_1, \mathbf{p}_1) + e_2(E_2, \mathbf{p}_2), \quad (1)$$

where E_0 , E_1 , and E_2 are energies, and \mathbf{p}_0 , \mathbf{p}_1 , and \mathbf{p}_2 are momenta of the incident and scattered and ejected electrons, respectively.

In the experiment the scattering kinematics is completely determined by measuring all necessary energies and angles associated with the above high-energy electron-impact ionization reaction. Neglecting the very small ion recoil energy and the thermal motion of the target, energy conservation requires that

$$\varepsilon = E_0 - E_1 - E_2, \quad (2)$$

where ε is the binding (ionization) energy of the target. Similarly conservation of momentum requires that

$$\mathbf{p} = \mathbf{p}_1 + \mathbf{p}_2 - \mathbf{p}_0. \quad (3)$$

The kinematics arrangement most used for EMS experiments is no-coplanar symmetric geometry in which the energies and polar angles of two outgoing electrons are equal ($E_1 = E_2$, $\theta_1 = \theta_2 = \theta = 45^\circ$) and the relative azimuthal angle between two outgoing electrons, $\phi = \pi - (\phi_2 - \phi_1)$, is

varied. Under these conditions the magnitude of target electron momentum is given by

$$p = \sqrt{(p_0 - 2p_1 \cos \theta)^2 + [2p_1 \sin \theta \sin(\phi/2)]^2}. \quad (4)$$

The details of our present EMS spectrometer have been described elsewhere [48]. Briefly, the no-coplanar symmetric geometry preferred for EMS is employed. The incident electron beam generated by an electron gun is accelerated by a lens system to the desired energy of 1200 eV plus the binding energy and transferred to the reaction region where the incident electron impacts with the gas-phase target molecule injected by a nozzle. The scattered and ejected electrons outgoing along the polar angle of 45° pass through a 90° sector of 2π spherical electrostatic analyzer, and are then detected in coincidence by a position-sensitive detector (PSD) placed at the exit plane of the analyzer. A multihit responsive PSD consisting of a pair of microchannel plates and a HEX120 delay line anode was applied recently to improve the detection efficiency [49].

The present experiment on CH_3I was carried out at the incident electron energy of 1200 eV plus binding energy with beam current of about 4.5 μA and an ambient pressure of 8×10^{-4} Pa. In order to achieve a better energy resolution, the electrons leaving the interaction region with ~ 600 eV energy are decelerated using retarding lenses and then analyzed at the reduced mean analyzer pass energy of 200 eV. The instrumental energy and momentum resolution were determined to be ~ 1.2 eV and ~ 0.18 a.u. ($\Delta\theta = 0.8^\circ$, $\Delta\phi = 2.2^\circ$), respectively, by measuring the Ar $3p$ orbital before and after the CH_3I experiment.

On the theoretical side, under the binary encounter and plane-wave impulse approximations (PWIA), as well as the Born-Oppenheimer approximation and further ignoring the contributions of molecular rotational and vibrational states, the EMS cross section for randomly oriented atoms or molecules can be expressed as [4]

$$\sigma_{\text{EMS}} = (2\pi)^4 \frac{p_1 p_2}{p_0} f_{ee} \frac{1}{4\pi} \int |\langle f | a(\mathbf{p}) | 0 \rangle|^2 d\Omega_{\mathbf{p}}, \quad (5)$$

where f_{ee} is the electron-electron collision factor which usually stays constant under the EMS experimental condition. $|0\rangle$ and $|f\rangle$ are electronic wave functions of the initial (ground) state of the neutral molecule and the final state of the molecular ion, respectively. $a(\mathbf{p})$ is the operator annihilating an electron of momentum \mathbf{p} . $\frac{1}{4\pi} \int d\Omega$ represents the spherical average over the random orientation of molecules.

With the weak-coupling approximation, the ion electronic state $|f\rangle$ can be expanded by the orthonormal basis states $|j\rangle$, which are the linear combinations of configurations formed by annihilating one electron in a target eigenstate [4]. The target-ion overlap is thus given by

$$\langle f | a(\mathbf{p}) | 0 \rangle = \sum_j \langle f | j \rangle \langle j | a(\mathbf{p}) | 0 \rangle. \quad (6)$$

Clearly $\langle j | a(\mathbf{p}) | 0 \rangle$ is zero if $|j\rangle$ is not a one-hole state $|i\rangle$ formed by annihilating an electron from the i th orbital in the target ground state. The weak-coupling expansion of the ion

state $|f\rangle$ subsequently leads to

$$\langle f|a(\mathbf{p})|0\rangle = \langle f|i\rangle\varphi_i(\mathbf{p}), \quad (7)$$

where $\varphi_i(\mathbf{p}) = \langle i|a(\mathbf{p})|0\rangle$ is the normalized Dyson orbital in momentum space.

Therefore the EMS cross section can be further expressed as

$$\sigma_{\text{EMS}} \propto \frac{1}{4\pi} S_f^i \int |\varphi_i(\mathbf{p})|^2 d\Omega_p, \quad (8)$$

where $S_f^i = |\langle f|i\rangle|^2$ is the spectroscopic factor or pole strength, the probability of finding a single-hole configuration in the final ion state. $\varphi_i(\mathbf{p})$ can be described by the canonical Hartree-Fock (HF) [4] or Kohn-Sham (KS) [50] orbital in molecular equilibrium geometry. Therefore, it is easy to see from Eq. (8) that EMS measurement is directly linked with the spherically averaged square of the modulus of the orbital wave function in momentum space, i.e., the electron-momentum profile. Equation (8) also suggests that the electron-momentum profiles for satellite states are identical in shape to that of the corresponding main transition, which forms the basis for the assignment of satellite states in EMS.

For heavy atoms or molecules containing heavy elements, relativistic effects could influence the electronic wave functions. Cook *et al.* successfully employed the Dirac-Fock wave function to describe the EMS experimental result of the Xe atom [26,27]. For molecules, four-component all-electron relativistic calculations are still difficult. Consequently, relativistic pseudopotential basis sets were the most commonly employed alternative for molecules containing high- Z atoms [31], but invalid for spin-orbit coupling effects. Recently the relativistic density functional (ADF) method [35,36] was introduced to the EMS studies [32–34], which can calculate two-component (spin-orbit coupling) and scalar relativistic MO wave functions, as well as the nonrelativistic one. The orbital wave function in position space generated by the spin-orbit relativistic method in the ADF program can be described as

$$\varphi_i(\mathbf{r}) = \varphi_\alpha(\mathbf{r})\alpha + \varphi_\beta(\mathbf{r})\beta, \quad (9)$$

where α and β are the spin variables which are orthogonal with each other, and $\varphi_\alpha(\mathbf{r})$ and $\varphi_\beta(\mathbf{r})$ are the relevant position space wave functions. Then, through Fourier transform, the cross section of EMS can be given by

$$\sigma_{\text{EMS}} \propto \frac{1}{4\pi} S_f^i \int [|\varphi_\alpha(\mathbf{p})|^2 + |\varphi_\beta(\mathbf{p})|^2] d\Omega_p, \quad (10)$$

where $\varphi_\alpha(\mathbf{p})$ and $\varphi_\beta(\mathbf{p})$ are the momentum space electron wave functions for the spin α and β components. S_f^i is the same as that in expression (8).

It is worth noting that the target-ion overlap in Eq. (5) can be also calculated by the SAC-CI general- R method [44–47], which has been used to study electron correlations of molecules in EMS [19–22]. The SAC-CI theory requires SAC calculation for the ground state and SAC-CI calculation for the ion states. For the singlet closed-shell state, the ground

state is defined by the SAC expansion as

$$\begin{aligned} |\Psi_0^{\text{SAC}}\rangle &= \exp\left(\sum_I C_I S_I\right)|0\rangle \\ &= \left(1 + \sum_I C_I S_I + \frac{1}{2} \sum_{I,J} C_I C_J S_I S_J + \dots\right)|0\rangle, \end{aligned} \quad (11)$$

where $|0\rangle$ is the HF determinant for the closed-shell ground state, S_I is the symmetry-adapted excitation operator, and C_I is the coefficient. The SAC wave functions well describe the electron correlation of the ground state. In the SAC-CI theory, the electron correlations in the final state are compactly described by considering some modifications to the ground-state electron correlations. The wave function of the final state is defined by using the SAC wave function as

$$|\Psi_f^{\text{SAC-CI}}\rangle = \Re |\Psi_0^{\text{SAC}}\rangle, \quad (12)$$

where the excitation operation \Re is defined as $\Re = \sum_k d_k R_k$. $\{R_k\}$ is a set of excitation, ionization, or electron-attached operators, and $\{d_k\}$ is the corresponding normalized coefficient set. For the multielectron processes, the operator \Re describes the excitation starting from the electron correlation involved in the SAC ground state, and can include up to sextuple excitations in the SAC-CI general- R method. Then the Dyson orbital constructed by SAC-CI theory is the linear combination of orthogonal HF orbitals,

$$\Psi_{\text{Dyson}} = \langle \Psi_f^{\text{SAC-CI}} | \Psi_0^{\text{SAC}} \rangle = \sum_j c_j \varphi_j^{\text{HF}}, \quad (13)$$

where φ_j^{HF} is the HF orbital with required symmetry and c_j is the expansion coefficient. The PS of this SAC-CI Dyson orbital is $S_f = \sum_j c_j^2$.

In the present work for CH_3I , nonrelativistic and spin-orbit relativistic calculations are performed to obtain the electron-momentum profiles of valence orbitals by using the ADF program [35,36] at a theoretical level of the B3LYP functional and quadruple-zeta basis sets with four polarization functions (QZ4P). For comparison, we also presented the B3LYP and HF calculations with aug-cc-pVTZ-PP basis set which include small-core energy-consistent relativistic pseudopotentials (PPs) for I [51] and aug-cc-pVTZ for C and H. In addition, the SAC-CI general- R method [44–46] with an aug-cc-pVTZ-PP basis set was used to calculate the ionization energies and pole strengths of the main transition states and satellite states, as well as the corresponding electron-momentum profiles. Since CH_3I belongs to the C_{3v} point group, which has degenerate π orbitals, the SAC-CI calculation is implemented in its nondegenerate subgroup C_s , and 100 and 40 ionized states are calculated for A' and A'' symmetries, respectively. These calculations are implemented with the GAUSSIAN09 program [52]. Note that the HF calculation only contained the electron exchange effect from the fermion nature while the B3LYP calculation considered both electron exchange and correlation interactions in the ground state of a neutral molecule through the hybrid exchange-correlation functionals. In the SAC-CI calculation, the

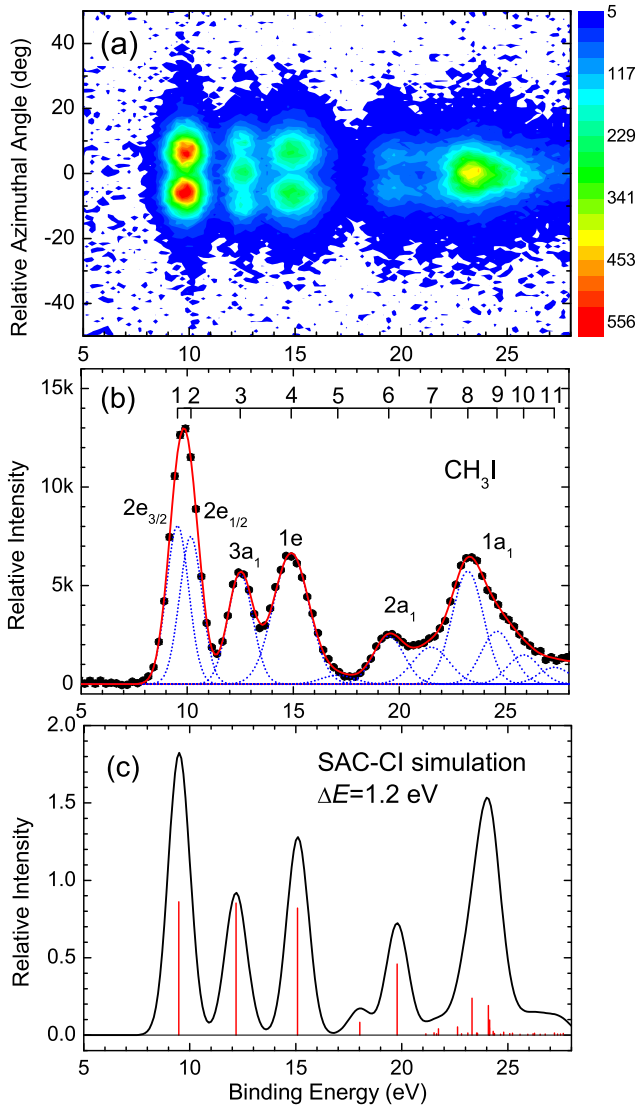


FIG. 1. (a) Two-dimensional electron density map of CH₃I. (b) Binding energy spectrum of CH₃I over all relative azimuthal angles. The dotted lines represent 11 Gaussian peaks used to fit the BES, and the solid line is the sum. (c) Simulated binding energy spectrum by SAC-CI general-*R*.

electron correlations in the initial and final states were taken into account.

III. RESULTS AND DISCUSSION

A. Binding energy spectra

The CH₃I molecule belongs to C_{3v} point group symmetry, and its ground-state electronic configuration in the single group representation can be written as (core)⁴⁸ $\underbrace{(1a_1)^2(2a_1)^2}_{\text{inner valence}} \underbrace{(1e)^4(3a_1)^2(2e)^4}_{\text{outer valence}}$. The spin-orbit coupling effect makes the ionization peak of the 2e orbital split into two components (2e_{3/2} and 2e_{1/2}) [37–42]. Figure 1(a) presents the two-dimensional electron density map (2D map) of CH₃I from the simultaneous measurement

on the binding energy and relative azimuthal angle. From the 2D map, different symmetries of valence orbitals can be identified clearly. The total BES obtained by integrating the 2D map over all relative azimuthal angles is displayed in Fig. 1(b). Three well-resolvable bands and two distinct spectral envelopes in the energy ranges of 8–17 eV and 17–28 eV are observed, which correspond to three outer valence orbitals (2e, 3a₁, 1e) and two inner valence orbitals (2a₁, 1a₁) together with their satellite lines. For the sake of comparison, the ionization energies (IEs) and pole strengths (PSs) of the main transition states and satellite states were calculated by the SAC-CI general-*R* method and presented in Table I together with the previous results [41–43]. The simulated BES employing the calculated IEs convoluting with our instrumental resolution of 1.2 eV is shown in Fig. 1(c). The positions and heights of the vertical bars represent the IEs and PSs of the corresponding Dyson orbitals calculated by the SAC-CI general-*R* method. The simulation can reproduce the feature of the presently measured BES well.

The first band of the BES corresponds to the ionizations from the HOMO 2e orbital. Due to the spin-orbit coupling effect, this band splits into two components (2e_{3/2} and 2e_{1/2}) with the energy separation of 0.6 eV observed in PES [41,42]. These two components cannot be resolved by the present EMS spectrometer with the energy resolution of 1.2 eV. In order to extract experimental EMPs for individual 2e_{3/2} and 2e_{1/2}, two Gaussian peaks [labeled 1 and 2 in Fig. 1(b)] are used to fit the BES at different azimuthal angles. The next two well-resolved bands (peaks 3 and 4) are related to the 3a₁ and 1e orbitals, respectively. Different from the outer valence region, the BES in the inner valence region exhibits two relatively broad envelopes from 17 to 28 eV. As indicated by the SAC-CI and ADC(3) calculations (see Table I), there are many satellite lines in the inner valence region. In our experimental and simulated BES, a weak structure around 17.1 eV, and a peak at 19.5 eV with a shoulder around 21.5 eV are observed, corresponding to the 2a₁ orbital ionization transition, which were also observed clearly in the high-resolution PES [41]. So three Gaussian functions (peaks 5–7) are introduced to fit the BES for the first inner valence envelope. To the last envelope, in view of the observation from the PES [41], we use four Gaussian peaks (peaks 8–11) to fit this broad envelope from the 1a₁ orbital ionization. In the deconvolution process, the peak positions of these Gaussian functions are referred to the high-resolution PES results [41]. The widths of the peaks are the Franck-Condon widths folded with our instrumental energy resolution [1.2 eV in full width at half maximum (FWHM)]. Small adjustments have been applied to compensate the shape asymmetries of the Franck-Condon profiles.

B. Electron-momentum profiles

The experimental EMPs for the 11 peaks are extracted by deconvoluting a series of azimuthal angular BES, and plotting the area of the corresponding fitted peak as a function of momentum p (i.e., ϕ). The results are presented in Figs. 2–6, together with the theoretical EMPs obtained by nonrelativistic and spin-orbit relativistic calculations with B3LYP/QZ4P, as well as relativistic pseudopotential

TABLE I. Ionization energies (IEs) (in eV), pole strengths (PSs), and the Dyson orbitals expanded with Hartree-Fock orbitals of valence ionized states for CH₃I.

MOs	EMS ^b	EMS [43]	PES [42]	PES [41]	SAC-CI general- <i>R</i> ^a			ADC(3) [41] (PS > 0.01)
					IP	PS (>0.005)	Dyson orbital expansion (C >0.04)	
$2e_{3/2}$	9.54 (0.86)	9.71 (>0.9)	9.540		9.50	0.864	$0.929(2e)^{-1}$	9.48 (0.92, $2e$)
$2e_{1/2}$	10.17 (0.86)		10.168					
$3a_1$	12.50 (0.85)	12.50 (>0.9)	12.5		12.18	0.854	$0.924(3a_1)^{-1}$	12.36 (0.91, $3a_1$)
$1e$	14.90 (0.82)	14.91 (>0.9)	14.7 15.4		15.09	0.822	$0.906(1e)^{-1}$	15.24 (0.88, $1e$)
$2a_1$	17.1 (0.06)			17.06	18.02	0.082	$0.276(2a_1)^{-1} + 0.070(1a_1)^{-1}$	16.68 (0.06, $2a_1$)
	19.5 (0.29)	20.0 (0.5)	19.5	19.46	19.78	0.459	$0.675(2a_1)^{-1} + 0.054(1a_1)^{-1}$	18.59 (0.50, $2a_1$)
	21.5 (0.28)		21.5	20.90	21.14	0.008	$0.064(2e)^{-1} + 0.059(1e)^{-1}$	20.24 (0.09, $2a_1$)
				21.56	21.52	0.015	$0.112(2a_1)^{-1} - 0.040(1a_1)^{-1}$	21.03 (0.04, $2a_1$)
					21.64	0.009	$0.094(2a_1)^{-1}$	
$1a_1$	23.2 (0.28)	23.9 (0.8)	23.2	23.21	22.63	0.053	$0.185(1a_1)^{-1} - 0.129(2a_1)^{-1}$	22.32(0.02, $1a_1$)
	24.6 (0.13)			24.49	22.81	0.008	$0.073(1a_1)^{-1}$	23.23(0.02, $2a_1$)
	25.9 (0.07)				23.11	0.014	$0.082(1a_1)^{-1} - 0.079(2a_1)^{-1}$	23.23(0.11, $1a_1$)
	27.3 (0.04)				23.31	0.239	$0.396(1a_1)^{-1} - 0.284(2a_1)^{-1}$	23.45(0.08, $1a_1$)
					23.53	0.014	$0.109(1a_1)^{-1} - 0.043(2a_1)^{-1}$	23.64(0.31, $1a_1$)
					23.57	0.012	$0.103(1a_1)^{-1}$	23.92(0.03, $1a_1$)
					24.08	0.192	$0.436(1a_1)^{-1}$	24.12(0.03, $1a_1$)
					24.14	0.048	$0.218(1a_1)^{-1}$	24.51(0.06, $1a_1$)
					24.14	0.097	$0.310(1a_1)^{-1}$	25.78(0.03, $2a_1$)
					24.31	0.024	$0.152(1a_1)^{-1}$	25.78(0.02, $1a_1$)
					24.37	0.011	$0.097(1a_1)^{-1} + 0.040(2a_1)^{-1}$	27.32(0.02, $1a_1$)
					24.66	0.006	$0.074(1a_1)^{-1}$	27.59(0.02, $1a_1$)
					24.81	0.019	$0.129(1a_1)^{-1} + 0.050(2a_1)^{-1}$	29.54(0.02, $2a_1$)
					25.09	0.009	$0.093(1a_1)^{-1}$	
					25.23	0.012	$0.102(1a_1)^{-1}$	
					25.58	0.006	$0.057(1a_1)^{-1} + 0.048(2a_1)^{-1}$	
					25.95	0.005	$0.048(1a_1)^{-1} + 0.040(2a_1)^{-1}$	
				26.19	0.008	$0.071(1a_1)^{-1} + 0.055(2a_1)^{-1}$		
				26.26	0.012	$0.079(1a_1)^{-1} + 0.075(2a_1)^{-1}$		
				26.53	0.006	$0.053(1a_1)^{-1} + 0.053(2a_1)^{-1}$		
				26.76	0.007	$0.058(1a_1)^{-1} + 0.057(2a_1)^{-1}$		
				27.19	0.014	$0.102(2a_1)^{-1} + 0.053(1a_1)^{-1}$		
				27.35	0.007	$0.071(2a_1)^{-1} + 0.044(1a_1)^{-1}$		
				27.49	0.006	$0.066(2a_1)^{-1} + 0.044(1a_1)^{-1}$		
				27.61	0.011	$0.084(2a_1)^{-1} + 0.061(1a_1)^{-1}$		

^aPresent calculation. Dyson orbitals with pole strengths greater than 0.005 are given here.

^bPresent experiment. The values in the parentheses are pole strengths which are determined by comparing the experimental EMPs with the theoretical ones calculated by relativistic B3LYP/QZ4P for other orbitals, assumed to be 0.86 for the $2e$ orbital according to the SAC-CI calculation.

calculations with B3LYP/aug-cc-pVTZ-PP and HF/aug-cc-pVTZ-PP. The error bars of the experimental data include both the statistical uncertainties and the uncertainties introduced during the deconvolution procedure. For the comparison with the experimental EMPs, the theoretical ones are folded with the instrumental momentum resolution of $\Delta\theta = 0.8^\circ$, $\Delta\phi = 2.2^\circ$ using the Gaussian weighted planar grid method [53]. The experimental and calculated EMPs are placed on a common intensity scale by normalizing the experimental EMP for the HOMO $2e$ orbital to the theoretical one; the pole strengths are assumed to be 0.86 according to the SAC-CI calculation. This factor will be as a reference to

determine the experimental pole strengths of ionizations for other orbitals.

Figure 2(a) shows the experimental and theoretical EMPs for the outermost $2e$ orbital. The orbital map in position space calculated by B3LYP/aug-cc-pVTZ-PP plotted in the figure shows that the $2e$ orbital is a typical iodine $5p$ lone-pair orbital. The experimental EMP for the $2e$ orbital displays an expected p -type character with a maximum at $p \sim 0.5$ a.u.. All the calculations can reproduce the experiment well. Figure 2(b) presents the individual EMPs for the spin-orbit splitting components $2e_{3/2}$ and $2e_{1/2}$. It is clearly shown in the figure that the experimental EMPs for the two

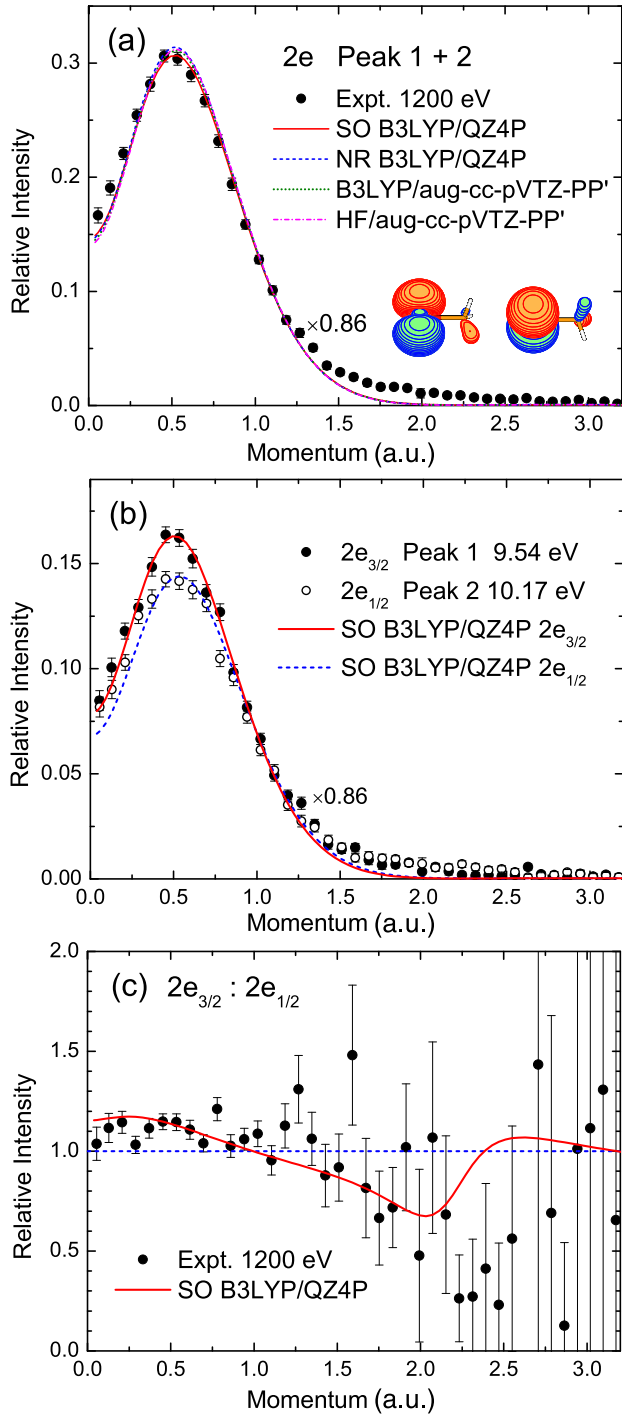


FIG. 2. (a) The experimental and theoretical EMPs for the HOMO $2e$ orbital, (b) those of two spin-orbit components $2e_{3/2}$ and $2e_{1/2}$, and (c) the ratio of $2e_{3/2}$ to $2e_{1/2}$. The orbital map in position space calculated by B3LYP/aug-cc-pVTZ-PP is also plotted in the figure. SO means spin-orbit relativistic calculation and NR represents nonrelativistic calculation.

components exhibit different intensities, being obviously greater for $2e_{3/2}$ than for $2e_{1/2}$ at the low-momentum region of $p < 1.0$ a.u., but the reversal happens in the high-momentum region of $p > 1.0$ a.u.. The spin-orbit relativistic calculations

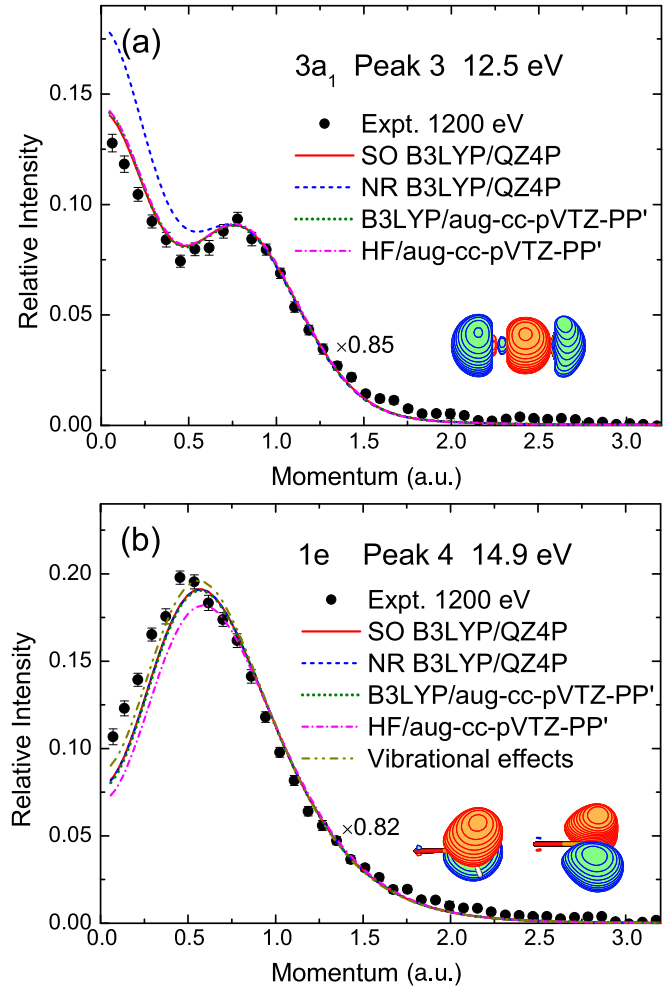


FIG. 3. The experimental and theoretical EMPs for (a) $3a_1$ and (b) $1e$ orbitals, together with their orbital maps in position space calculated by B3LYP/aug-cc-pVTZ-PP.

(SO B3LYP/QZ4P) can reproduce their distinguishable profiles very well. The experimental branching ratio of $2e_{3/2}$: $2e_{1/2}$ is plotted in Fig. 2(c). It varies obviously along with momentum increasing which deviates from nonrelativistic theoretical prediction, namely, 1:1. However, the branching ratio given by the spin-orbit relativistic calculations is well consistent with the experiment. These observable results indicate the noticeable relativistic effects on the wave functions for $2e_{3/2}$ and $2e_{1/2}$.

The experimental EMPs for two well-resolved bands (peak 3 at 12.5 eV and peak 4 at 14.9 eV) in BES are depicted in Fig. 3. As described above, these two bands are well assigned to $3a_1$ and $1e$ outer valence orbitals, respectively. Correspondingly the calculated results for them are also plotted in the figure for comparison. It can be seen from Fig. 3(a) that the measured EMP of $3a_1$ exhibits s - p type character with high intensity at $p \sim 0$ and a shoulder at $p \sim 0.8$ a.u.. The nonrelativistic calculation overestimates the experimental intensity remarkably at the low-momentum region. Nevertheless, the calculations using the relativistic B3LYP/QZ4P or the HF and B3LYP with the relativistic pseudopotential basis set of aug-cc-pVTZ-PP are in good agreement with the experiment,

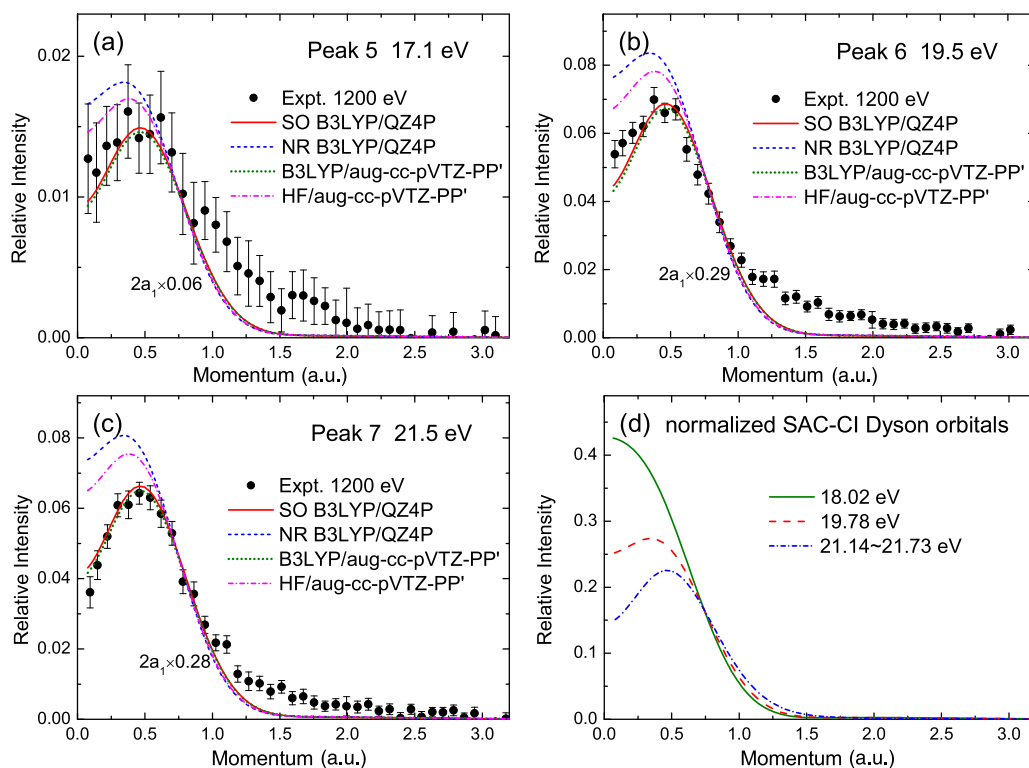


FIG. 4. The experimental EMPs for satellite lines (peaks 5–7) and the calculated ones for the $2a_1$ inner valence orbital: (a) peak 5, (b) peak 6, and (c) peak 7. (d) The SAC CI general- R calculations for the states in three corresponding ionization energy regions.

indicating the significant relativistic effect on the $3a_1$ orbital. It is easily understandable for the presence of relativistic effects in view of the C-I bonding character as the $3a_1$ orbital map shows. It is noted that all the theoretical profiles for the $3a_1$ orbital have been multiplied by a factor of 0.85 in comparison with the measurement. This factor represents the pole strength for the one-hole state of ionization from the $3a_1$ orbital and well agrees with the SAC-CI prediction.

For peak 4 in BES (14.9 eV), ionized from the doubly degenerate $1e$ orbital, the experimental and theoretical EMPs are shown in Fig. 3(b). They are p -type momentum profiles with a maximum at $p \sim 0.5$ a.u.. The calculation by the HF method with the pseudopotential basis set seriously underestimates the experimental data in the low-momentum region. This discrepancy is substantially improved by using B3LYP with the same basis set, which suggests the outcome of electron correlation effects in the initial state. Compared with the nonrelativistic and relativistic B3LYP results, these calculations display the same profiles and can explain the experimental shape well, but underestimate the intensity at small momentum. It is apparent that the relativistic effects are absent for this orbital dominated by methyl electrons as the orbital map displays. Besides, the pole strength for the $1e$ orbital is identified as 0.82, which agrees with the SAC-CI calculation.

It is noted that there still existed a small discrepancy between the experimental EMP and the theoretical ones for the $1e$ orbital at the low-momentum region. One possible reason for the unexpected intensity is the result of the molecular vibrational effect which was considered in recent EMS studies [54–61]. Watanabe *et al.* proposed a harmonic analytical quantum mechanical (HAQM) approach [56,57] to investigate

the influence of vibrational modes, in which the final EMP is equivalent to the one at the equilibrium geometry plus the sum of contributions from every vibrational mode. We used the HAQM method to calculate the EMP considering vibrational effects and plotted it in Fig. 3(b). One can see that it slightly improves the intensity in the low-momentum region. The remaining deviation between experiment and theory may be attributed to the distorted wave effect, which was proposed to explain the unexpected high intensity at the low-momentum region in EMS studies [62–66].

In the inner valence region, according to the SAC-CI calculation, the peaks (5, 6, 7) in the BES at 17.1, 19.5, and 21.5 eV represent three satellite lines of the $2a_1$ orbital with different configurations. The experimental EMPs for the satellites along with the calculated one for the $2a_1$ orbital are presented in Figs. 4(a)–4(c), respectively. The spin-orbit relativistic and pseudopotential B3LYP calculations can generally depict the experimental data when multiplied by a suitable factor. Such factors, i.e., the pole strengths for the three satellites, are estimated to be 0.06, 0.29, and 0.28, respectively. However, the nonrelativistic B3LYP and the pseudopotential HF calculations multiplied by the same factors still seriously overestimate the experimental intensity at small momentum. The experimental and theoretical results indicate that the EMPs for the $2a_1$ orbital and its satellites are quite sensitive to the relativistic effect and electron correlation effects.

It is worth noting that the measured EMPs for these three satellites show diverse shapes and their intensities decrease gradually in the low-momentum region as the ionization energies increase. This phenomenon is very different from previous EMS observations [5–20] that the EMPs for satellite states

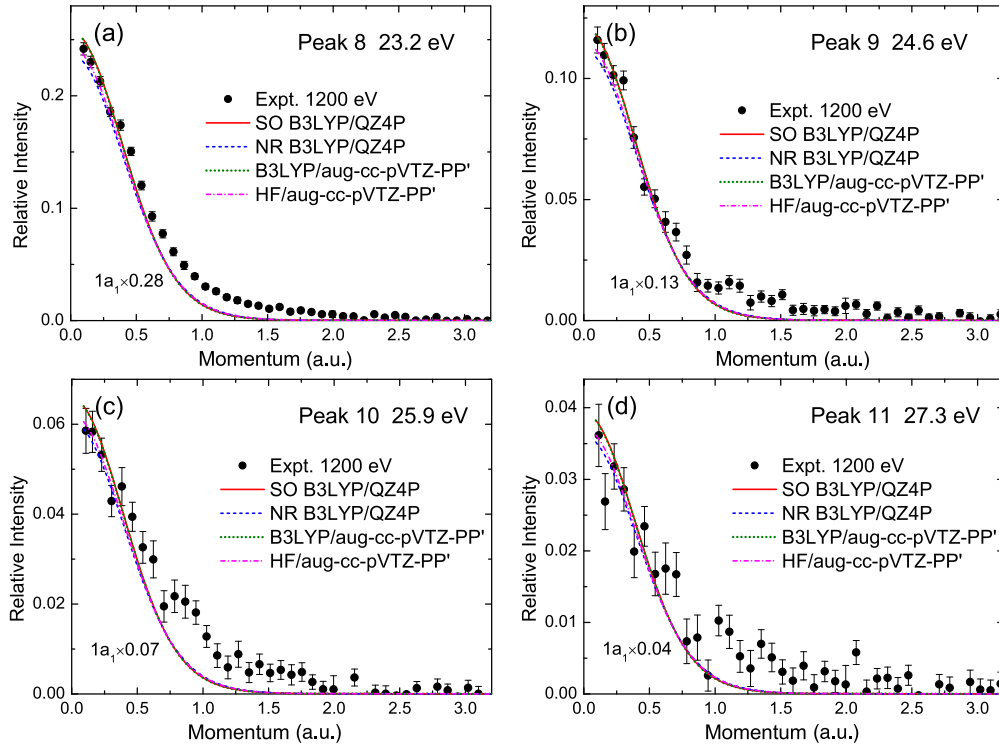


FIG. 5. The experimental EMPs for satellite lines (peaks 8–11) and the calculated one for the $1a_1$ inner valence orbital: (a) peak 8, (b) peak 9, (c) peak 10, and (d) peak 11.

are of indistinguishable shapes from the main (parent) ionization state. In order to know the source of the difference, we employ the SAC-CI general- R method to calculate the Dyson orbitals and their corresponding momentum profiles. The normalized SAC-CI profiles for the states in three ionization energy regions, corresponding to three experimental satellites, are displayed in Fig. 4(d). With the ionization energies increasing, lower and lower intensities of the theoretical profiles at the low-momentum region give a rational explanation of the experimental results. The appearance of different profiles for the $2a_1$ satellites reveals that electron correlation effects have a notable impact on ionization transitions and may result in the mixture of inner valence states with the same symmetry as the Dyson orbital expansion listed in Table I. The interaction of $2a_1$ and $1a_1$ ionization configurations should be responsible for the present observation. It suggests that careful analysis must be taken to investigate electron-momentum profiles for satellite lines, rather than simple thinking about them with the same shapes as that of parent states.

In the binding energy region of 22–28 eV, four peaks (peaks 8–11) are used to fit the last envelope of BES. The SAC-CI calculation suggested they belong to the $1a_1$ orbital ionization state and its satellites. The corresponding EMPs together with the calculations for the $1a_1$ orbital are plotted in Fig. 5. They all exhibit s -type characters with a maximum at $p = 0$. As shown in Table I, the coefficients of $2a_1$ in the Dyson orbitals expansion of the $1a_1$ satellite configurations are relatively small, so the theoretical momentum profiles for the $1a_1$ orbital can explain the experimental data with the pole strength of 0.28 for peak 8 at 23.2 eV, 0.13 for peak 9 at 24.6 eV, 0.07 for peak 10 at 25.9 eV, and 0.04 for peak 11 at 27.3 eV. Such serious splitting of the pole strengths

indicates the strong electron correlation in the final ion states.

For the satellite lines of $2a_1$ and $1a_1$ inner valence orbitals, in order to eliminate the possible uncertainty from the deconvolution process in fitting the BES, the summed EMPs of peaks 5–7 for $2a_1$ satellites and peaks 8–11 for $1a_1$ satellites are plotted in Fig. 6, as well as the calculated EMPs and orbital maps for $2a_1$ and $1a_1$ orbitals. One can see from Fig. 6(a) that only relativistic and pseudopotential B3LYP calculations can reproduce the experiment well when multiplied by the factor of 0.63, again indicating the significance of relativistic effects and electron correlation effects in the $2a_1$ orbital. It is noted that the experimental pole strengths of 0.06, 0.29, and 0.28 for the three $2a_1$ satellites, respectively, are not in accordance with the present SAC-CI and previous ADC(3) [41] calculations, but the summed pole strength of 0.63 well agrees with the theoretical prediction. As for the four $1a_1$ satellites, as shown in Fig. 6(b), the calculated EMPs of the $1a_1$ orbital can describe the summed experimental EMP when multiplied by the summed pole strength of 0.53. The pole strengths for the four $1a_1$ satellites, particular to their sum, are generally predicted by the calculations.

IV. CONCLUSION

A high-statistics EMS measurement of CH_3I at electron-impact energy of 1.2 keV plus binding energy has been reported. The experimental binding energy spectrum is well simulated by the SAC-CI calculation. The experimental EMPs for valence orbitals of CH_3I are compared with the nonrelativistic and spin-orbit relativistic B3LYP calculations, as well as relativistic pseudopotential calculations. The relativistic

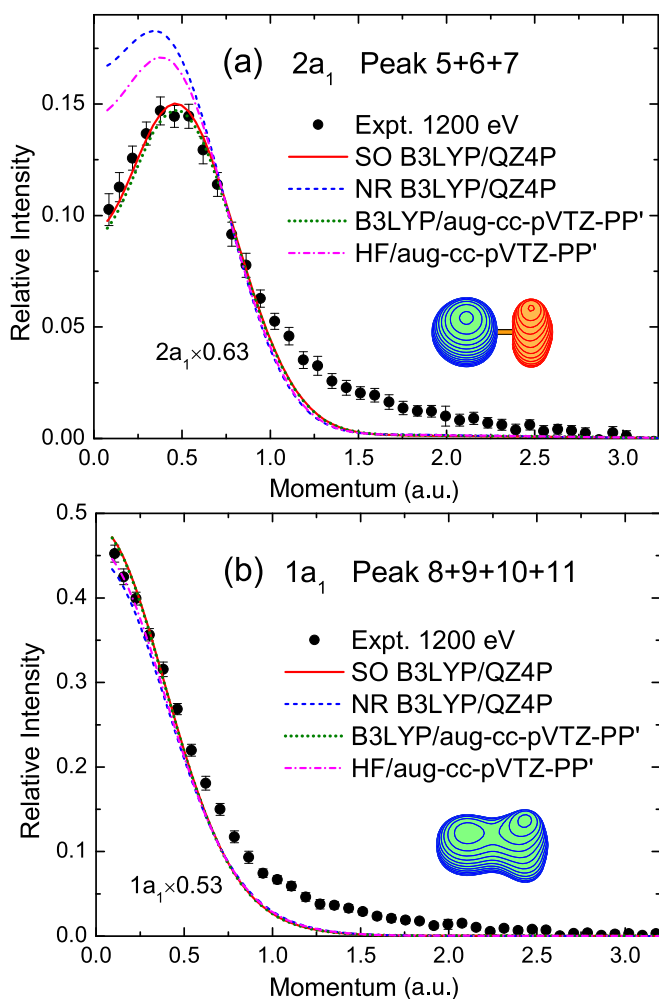


FIG. 6. The summed EMPs for satellite lines of $2a_1$ and $1a_1$ inner valence orbitals, together with the calculated EMPs and orbital maps for $2a_1$ and $1a_1$.

B3LYP calculation interpreted the measured EMPs for two spin-orbit splitting components $2e_{3/2}$ and $2e_{1/2}$ quite well, as well as that of the C-I bonding $3a_1$ orbital. In the inner valence region, the measured EMPs for three $2a_1$ satellites and four $1a_1$ satellites are extracted and the experimental pole strengths for these satellites are determined. Serious splitting of pole strengths for $2a_1$ and $1a_1$ ionizations is found, indicating the presence of strong electron correlation effects in the final ion states, which is associated with the ionization and shake-up excitation processes of electrons. It is worth noting that for the inner valence orbital $2a_1$ and its satellites the distinct relativistic effects and electron correlation effects are found through the comparison of the experimental and calculated results. The difference between the HF and B3LYP calculations reveals the noticeable electron correlation in the initial ground state of the neutral molecule. In addition, the appearance of different EMP shapes for three $2a_1$ satellites can be explained qualitatively by the SAC-CI general- R calculation, which illustrates the configuration mixture of inner valence orbitals induced by the initial- and final-state electron correlation effects. The present study demonstrated that relativistic effects and electron correlation effects play important roles in the electronic structure of molecules containing heavy elements.

ACKNOWLEDGMENTS

This work was supported by the National Natural Science Foundation of China (Grants No. 11534011, No. 11874339, and No. 11804328) and the Fundamental Research Funds for the Central Universities (Grant No. WK2030040094). The authors also gratefully acknowledge Professor C. E. Brion from the University of British Columbia (UBC) in Canada for giving us the HEMS programs. The SAC-CI calculation with GAUSSIAN09 program was performed on the supercomputing system in the Supercomputing Center of University of Science and Technology of China.

- [1] I. E. McCarthy and E. Weigold, *Rep. Prog. Phys.* **54**, 789 (1991).
- [2] C. E. Brion, *Int. J. Quantum Chem.* **29**, 1397 (1986).
- [3] M. A. Coplan, J. H. Moore, and J. P. Doering, *Rev. Mod. Phys.* **66**, 985 (1994).
- [4] E. Weigold and I. E. McCarthy, *Electron Momentum Spectroscopy* (Kluwer Academic, Plenum, New York, 1999).
- [5] L. S. Cederbaum, J. Schirmer, W. Domcke, and W. von Niessen, *J. Phys. B: At. Mol. Phys.* **10**, L549 (1977).
- [6] L. S. Cederbaum, W. Domcke, J. Schirmer, and W. Von Niessen, in *Correlation Effects in the Ionization of Molecules: Breakdown of the Molecular Orbital Picture*, edited by I. Prigogine and S. A. Rice, Advances in Chemical Physics (John Wiley & Sons, Ltd, 1986), Vol. 65, p. 115.
- [7] P. Roy, I. Nenner, P. Millie, P. Morin, and D. Roy, *J. Chem. Phys.* **84**, 2050 (1986).
- [8] M. S. Deleuze, A. B. Trofimov, and L. S. Cederbaum, *J. Chem. Phys.* **115**, 5859 (2001).
- [9] M. Ehara, M. Ishida, and H. Nakatsuji, *J. Chem. Phys.* **117**, 3248 (2002).
- [10] M. Ehara, Y. Ohtsuka, H. Nakatsuji, M. Takahashi, and Y. Udagawa, *J. Chem. Phys.* **122**, 234319 (2005).
- [11] O. Samardzic, S. W. Braidwood, E. Weigold, and M. J. Brunger, *Phys. Rev. A* **48**, 4390 (1993).
- [12] I. E. McCarthy, R. Pascual, P. Storer, and E. Weigold, *Phys. Rev. A* **40**, 3041 (1989).
- [13] R. Nicholson, S. W. Braidwood, I. E. McCarthy, E. Weigold, and M. J. Brunger, *Phys. Rev. A* **53**, 4205 (1996).
- [14] S. Braidwood, M. Brunger, and E. Weigold, *Phys. Rev. A* **47**, 2927 (1993).
- [15] W. von Niessen, M. J. Brunger, and E. Weigold, *J. Phys. B: At. Mol. Phys.* **27**, 4309 (1994).
- [16] M. Takahashi, K. Otsuka, and Y. Udagawa, *Chem. Phys.* **227**, 375 (1998).
- [17] M. S. Deleuze and S. Knippenberg, *J. Chem. Phys.* **125**, 104309 (2006).
- [18] X. Shan, X. J. Chen, L. X. Zhou, Z. J. Li, T. Liu, X. X. Xue, and K. Z. Xu, *J. Chem. Phys.* **125**, 154307 (2006).
- [19] C. W. Huang, X. Shan, Z. Zhang, E. L. Wang, Z. J. Li, and X. J. Chen, *J. Chem. Phys.* **133**, 124303 (2010).

- [20] Q. Tian, J. Yang, Y. Shi, X. Shan, and X. Chen, *J. Chem. Phys.* **136**, 094306 (2012).
- [21] Y. R. Miao, C. G. Ning, K. Liu, and J. K. Deng, *J. Chem. Phys.* **134**, 204304 (2011).
- [22] Y. R. Miao, C. G. Ning, and J. K. Deng, *Phys. Rev. A* **83**, 062706 (2011).
- [23] K. S. Pitzer, *Acc. Chem. Res.* **12**, 271 (1979).
- [24] P. Pyykko and J. P. Desclaux, *Acc. Chem. Res.* **12**, 276 (1979).
- [25] P. Pyykko, *Chem. Rev.* **88**, 563 (1988).
- [26] J. P. D. Cook, J. Mitroy, and E. Weigold, *Phys. Rev. Lett.* **52**, 1116 (1984).
- [27] J. P. D. Cook, I. E. McCarthy, J. Mitroy, and E. Weigold, *Phys. Rev. A* **33**, 211 (1986).
- [28] L. Frost, J. Mitroy, and E. Weigold, *J. Phys. B: At. Mol. Phys.* **19**, 4063 (1986).
- [29] J. Bonfert, H. Graf, and W. Nakel, *J. Phys. B: At. Mol. Phys.* **24**, 1423 (1991).
- [30] X. G. Ren, C. G. Ning, J. K. Deng, G. L. Su, S. F. Zhang, and Y. R. Huang, *Phys. Rev. A* **73**, 042714 (2006).
- [31] Z. J. Li, X. J. Chen, X. Shan, X. X. Xue, T. Liu, and K. Z. Xu, *Chem. Phys. Lett.* **457**, 45 (2008).
- [32] K. Liu, C. G. Ning, and J. K. Deng, *Phys. Rev. A* **80**, 022716 (2009).
- [33] J. S. Zhu, J. K. Deng, and C. G. Ning, *Phys. Rev. A* **85**, 052714 (2012).
- [34] E. L. Wang, Y. F. Shi, X. Shan, H. J. Yang, W. Zhang, and X. J. Chen, *Chin. J. Chem. Phys.* **27**, 503 (2014).
- [35] G. Te Velde, F. M. Bickelhaupt, E. J. Baerends, C. Fonseca Guerra, S. J. van Gisbergen, J. G. Snijders, and T. Ziegler, *J. Comput. Chem.* **22**, 931 (2001).
- [36] C. F. Guerra, J. Snijders, G. te Velde, and E. Baerends, *Theor. Chem. Acc.* **99**, 391 (1998).
- [37] A. W. Potts, H. J. Lempka, D. G. Streets, and W. C. Price, *Philos. Trans. R. Soc., A* **268**, 59 (1970).
- [38] K. Leif, J. Reinhard, M. Lars, C. Foo Tim, and S. Kai, *Phys. Scr.* **16**, 225 (1977).
- [39] T. A. Carlson, A. Fahlman, M. O. Krause, P. R. Keller, J. W. Taylor, T. Whitley, and F. A. Grimm, *J. Chem. Phys.* **80**, 3521 (1984).
- [40] K. Kimura, S. Katsumata, Y. Achiba, T. Yamazaki, and S. Iwata, *Handbook of HeI Photoelectron Spectra of Fundamental Organic Molecules* (Halsted Press, New York, 1981).
- [41] D. M. P. Holland, I. Powis, G. Öhrwall, L. Karlsson, and W. von Niessen, *Chem. Phys.* **326**, 535 (2006).
- [42] W. von Niessen, L. Åsbrink, and G. Bieri, *J. Electron Spectrosc. Relat. Phenom.* **26**, 173 (1982).
- [43] A. Minchinton, J. Cook, E. Weigold, and W. Von Niessen, *Chem. Phys.* **93**, 21 (1985).
- [44] H. Nakatsuji, *Chem. Phys. Lett.* **177**, 331 (1991).
- [45] H. Nakatsuji, *J. Chem. Phys.* **83**, 713 (1985).
- [46] H. Nakatsuji, *J. Chem. Phys.* **83**, 5743 (1985).
- [47] H. Nakatsuji, *J. Chem. Phys.* **94**, 6716 (1991).
- [48] Q. Tian, K. Wang, X. Shan, and X. Chen, *Rev. Sci. Instrum.* **82**, 033110 (2011).
- [49] Y. Tang, X. Shan, S. Niu, Z. Liu, E. Wang, N. Watanabe, M. Yamazaki, M. Takahashi, and X. Chen, *J. Phys. Chem. A* **121**, 277 (2017).
- [50] P. Duffy, D. P. Chong, M. E. Casida, and D. R. Salahub, *Phys. Rev. A* **50**, 4707 (1994).
- [51] K. A. Peterson, B. C. Shepler, D. Figgien, and H. Stoll, *J. Phys. Chem. A* **110**, 13877 (2006).
- [52] M. J. Frisch, G. W. Trucks, H. B. Schlegel, G. E. Scuseria, M. A. Robb, J. R. Cheeseman, G. Scalmani, V. Barone, B. Mennucci, G. A. Petersson *et al.*, GAUSSIAN09, Gaussian, Inc., 2009.
- [53] P. Duffy, M. E. Cassida, C. E. Brion, and D. P. Chong, *Chem. Phys. Lett.* **159**, 347 (1992).
- [54] B. Hajgató, M. S. Deleuze, and F. Morini, *J. Phys. Chem. A* **113**, 7138 (2009).
- [55] K. Liu, C. G. Ning, Z. H. Luo, L. L. Shi, and J. K. Deng, *Chem. Phys. Lett.* **497**, 229 (2010).
- [56] N. Watanabe, M. Yamazaki, and M. Takahashi, *J. Chem. Phys.* **137**, 114301 (2012).
- [57] N. Watanabe, M. Yamazaki, and M. Takahashi, *J. Chem. Phys.* **141**, 244314 (2014).
- [58] Y. Tang, X. Shan, J. Yang, S. Niu, Z. Zhang, N. Watanabe, M. Yamazaki, M. Takahashi, and X. Chen, *J. Phys. Chem. A* **120**, 6855 (2016).
- [59] F. Morini, M. S. Deleuze, N. Watanabe, and M. Takahashi, *J. Chem. Phys.* **142**, 094308 (2015).
- [60] F. Morini, N. Watanabe, M. Kojima, M. S. Deleuze, and M. Takahashi, *J. Chem. Phys.* **143**, 134309 (2015).
- [61] M. Farasat, S. H. R. Shojaei, F. Morini, M. M. Golzan, and M. S. Deleuze, *J. Phys. B: At., Mol. Opt. Phys.* **49**, 075102 (2016).
- [62] I. McCarthy, *Aust. J. Phys.* **48**, 1 (1995).
- [63] C. E. Brion, Y. Zheng, J. Rolke, J. J. Neville, I. E. McCarthy, and J. Wang, *J. Phys. B: At., Mol. Opt. Phys.* **31**, L223 (1998).
- [64] X. G. Ren, C. G. Ning, J. K. Deng, S. F. Zhang, G. L. Su, F. Huang, and G. Q. Li, *Phys. Rev. Lett.* **94**, 163201 (2005).
- [65] C. G. Ning, X. G. Ren, J. K. Deng, G. L. Su, S. F. Zhang, and G. Q. Li, *Phys. Rev. A* **73**, 022704 (2006).
- [66] Y. Miyake, M. Takahashi, N. Watanabe, Y. Khajuria, Y. Udagawa, Y. Sakai, and T. Mukoyama, *Phys. Chem. Chem. Phys.* **8**, 3022 (2006).